Magnets Shifting Design of Dual PM Excited Vernier Machine for High-torque Application*

Feilong Yan, *Jinghua Ji**, *Zhijian Ling*, *Yuhua Sun and Wenxiang Zhao*
(School of Electrical and Information Engineering, Jiangsu University, Zhenjiang 212013, China)

Abstract: In this study, a novel dual permanent magnet excited vernier machine (DPMEVM) with magnets shifting in stator is proposed. Compared with the conventional permanent magnet synchronous machine (PMSM), the DPMEVM based on the bidirectional field modulation effect can operate in a wider torque range. However, the torque ripple of a conventional DPMEVM is high because of the superposition of the torque generated by the stator-side and rotor-side PMs. Consequently, a novel DPMEVM with magnets shifting is proposed to further reduce the torque ripple. First, the topologies and working principles of the baseline machine and proposed machines are introduced. Second, the torque-contribution harmonics are analyzed and calculated using the Maxwell tensor method. The calculation results reveal that the DPMEVM, benefiting from multiple working harmonics, can offer an enhanced torque capability compared to the PMSM. In addition, the torque ripple characteristics of the proposed machines are analyzed. It is verified that the torque ripple can be significantly reduced through magnets shifting. Third, the performances of the baseline machine and proposed machines are analyzed and compared in terms of flux density, open-circuit back-EMF, and torque characteristics. In addition, the proposed principle can be extended to machines with the same unit motor. Finally, a 120s-110p prototype machine is manufactured for validation.

Keywords: Permanent magnet vernier machine, bidirectional field modulation effect, magnets shifting, multiple working harmonics, torque

1 Introduction

Permanent magnet (PM) synchronous machines (PMSMs) have been extensively applied in the past decades owing to their advantages of high torque density and efficiency. They can be a promising candidate for high-torque fields such as wind power generation, electric vehicles, and ship propulsion [1-3]. Despite these merits of PMSMs, they suffer from high PM usage, which greatly restricts their application and performance. Recently, PM vernier machines (PMVMs) have been studied by researchers because of their high torque density, which makes them more suitable for direct-drive applications [4-5]. The reason why PMVMs can obtain high torque density is the "magnetic field modulation effects" that have been analyzed in details [6-8].

PMVMs can be categorized into stator-PM and rotor-PM machines according to the placement of the PMs. Both the stator-PM and rotor-PM PMVMs can adopt the same PM structure, which include surface mounted [9-10], spoke-array [11-12], Halbach type [13-14] and consequent pole [15-16] (CP). The difference between these machines is that the rotor pole pairs of the PMVMs are not equal to the winding pole pairs. Moreover, the stator teeth always adopt a split tooth structure to increase the modulation ratio [17]. The PMVM can produce a higher average torque than a PMSM with the same N-S structure. The split tooth structure achieves a higher torque density than the straight tooth structure, which was analyzed in Ref. [18]. Compared with the N-S pole structure, the spoke array [12] and Halbach type [19] can obtain a higher torque density. The CP structure was first applied in Ref. [20], which has many advantages over N-S poles. Moreover, the CP structure can produce a higher torque density than N-S poles as well [21].

Dual PM excited vernier machines (DPMEVMs) with PMs in both the stator and rotor are proposed and

Manuscript received November 1, 2021; revised February 26, 2022; accepted March 30, 2022. Date of publication September 30, 2022; date of current version June 16, 2022.

* Corresponding Author, E-mail: jjh@ujs.edu.cn

* Supported by the National Natural Science Foundation of China under Grant 52025073, and the Natural Science Foundation of Jiangsu Province under Grant BK20210770.

Digital Object Identifier: 10.23919/CJEE.2022.000028

studied owing to their high torque density. In Ref. [22], a DPME machine was proposed and analyzed for the first time. However, owing to their poor properties, PM materials have received little attention. A novel dual-PM-excited machine with PMs in both the rotor and stator was proposed in Ref. [23]. This structure can significantly improve the torque density. However, this complex structure causes manufacturing difficulties. In Ref. [24], a novel PMVM with Halbach array PMs employed in the stator slot opening was proposed. When a consequent pole was employed in the rotor, it was shown that the structure could produce a 54.8% higher torque than the N-S poles. However, the torque ripple of the proposed machine remains high. The slot-pole combination of the split tooth structure of DPMEVM was analyzed and compared in Ref. [10]; however, the working harmonic analysis was insufficient. Four types of dual-PM machines were compared in Ref. [25], whose harmonics were analyzed as well. However, the torque was not analyzed. In this study, a novel DPMEVM with magnets shifting in stator is proposed to further reduce the torque ripple. The working harmonics of the DPMEVMs were analyzed based on the magnetic field modulation effect. Meanwhile, the torque produced by each working harmonic was calculated using the Maxwell tensor method. In addition, the principle of torque ripple reduction was analyzed and verified.

The remainder of this paper is organized as follows. In Section 2, the operating principle is introduced based on the unit motor. The PM and dual three-phase winding magnetic motive force (MMF) are investigated. Meanwhile, the air gap flux density of the PMs and wingdings are derived, and the torque generation mechanism is introduced. In addition, the working principle of the torque ripple reduction is analyzed. In Section 3, the performances of three different machines are compared, including the flux density, open-circuit back electromotive force (EMF), and torque characteristics. Especially, the torque produced by each working harmonic is calculated. Additionally, the magnets shifting in the stator technique in the proposed machine is analyzed. Subsequently, the revealed principle is extended into the 120s-110p models of PMSM and DPMEVM with the same unit motor of 24s-22p. Finally, a prototype of the 120s-110p PMSM is manufactured for validation.

2 Operation principle

To facilitate the analysis, first the unit motor of 24s-22p is chosen and analyzed. The 120s-110p models are elaborated in Section 3.5. Fig. 1 shows the cross sections of the existing and proposed machines. All three machines adopt a dual three-phase with a 30° phase shift. As shown in Fig. 1a, the conventional PMSM adopts N-S poles, and the number of winding pole pairs is the same as that of the rotor pole pairs. Figs. 1b and 1c depict the structure of the proposed DPMEVMs. The PMs of the proposed machines are embedded in both the rotor and the stator. As can be seen, the structures of proposed machines I and Ⅱ are almost identical. The difference is that all the stator PMs are shifted by the same angle β in proposed machine Ⅱ. The rotor and stator adopt a CP structure in which only N-pole PMs exist. One N-pole PM can be considered as a pair of magnetic poles. Hence, there are only 37 PMs in the rotor. The rotor and stator both have flux modulation poles (FMPs). The number of rotor FMPs is 37, which is the same as that of the rotor PM pole pairs. The stator has 48 FMPs, which are formed by a stator split-tooth structure. There are 24 PM arrays in the slots formed by stator side FMPs. The main structural parameters of these three machines are listed in Tab. 1.

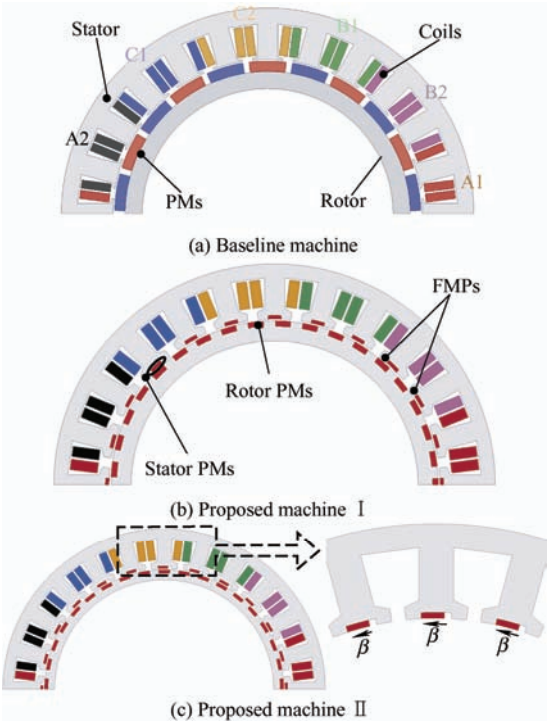

Fig. 1 Cross sections of the analyzed machines

Tab. 1 Parameters of three machines

Parameter	Baseline machine	Proposed machine Ⅰ	Proposed machine Ⅱ
PM pole-pairs	11	37	37
Winding pole-pairs		11	
Stator outer diameter/mm		260	
Stator inner diameter/mm		180	
Axial length/mm		70	
Air-gap length/mm		1	

2.1 Magnetic motive force

The PMSM and DPMEVMs have different PM structures, and so do the PM MMF and permeance; consequently, the air gap flux density is discrepant.

Fig. 2 shows the rotor PM MMF of the two rotor structures. Their PM MMF expressions can be obtained using Fourier decomposition. The rotor PM MMF $F_{rpm}(\theta_s,t)$ of the PMSM can be expressed as

$$F_{rpm}(\theta_s,t)=\sum_{i=1,3,5,\cdots}^{\infty} F_i \cos ip_{rpm}(\theta_s-\omega_r t) \tag{1}$$

where F_i is the amplitude of i^{th} order harmonic. p_{rpm} denotes rotor PM pole pair number. ω_r is the mechanical rotating velocity and θ_s is the mechanical angle.

The rotor PM MMF $F_{rpm}(\theta_s,t)$ of the DPMEVMs can be expressed as

$$F_{rpm}(\theta_s,t)=F_0+\sum_{j=1,2,3,\cdots}^{\infty} F_j \cos ip_{rpm}(\theta_s-\omega_r t) \tag{2}$$

The stator PM MMF $F_{spm}(\theta_s)$ of the DPMEVMs can be expressed as

$$F_{spm}(\theta_s)=F_{s0}+\sum_{j=1,2,3,\cdots}^{\infty} F_{sj}\cos jZ\theta_s \tag{3}$$

where F_{s0} and F_{sj} are the DC component and amplitude of the j^{th} order harmonics, respectively. Z denotes stator slots.

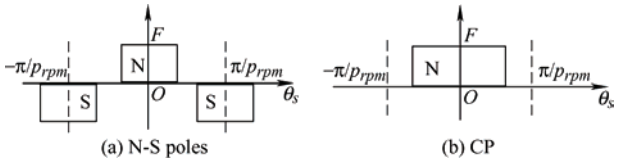

Fig. 2 The PM MMF distribution of two rotor structures

The PMSM and DPMEVMs have the same winding configuration, and the winding MMF $F_s(\theta_s,t)$ can be expressed as

$$F_s(\theta_s,t)=\sum_{h}^{\infty} F_h\cos(p_{rpm}\omega_r t-h\theta_s)+\sum_{k}^{\infty} F_k\cos(p_{rpm}\omega_r t+k\theta_s) \tag{4}$$

where h and k are positive integers and F_h and F_k are the corresponding amplitudes.

Compared with three-phase machines, dual three-phase machines can reduce the torque ripple and enhance fault-tolerance capability as well as torque density. The different phase-shift angles between the two winding sets have an important influence on the electromagnetic performance. This is mainly owing to the different harmonic contents of the winding MMF. The v^{th} harmonic is eliminated when it satisfies

$$\begin{cases} v(\gamma_{k+1}-\gamma_k)+\alpha=\pm 180°+n\times 360° \\ v(\gamma_{k+1}-\gamma_k)-\alpha=\pm 180°+n\times 360° \end{cases} \tag{5}$$

where γ_k and γ_{k+1} are the phase angles of the k^{th} and $(k+1)^{\text{th}}$ order harmonics, respectively. α is the phase shift angle between the two winding sets.

Fig. 3 shows the winding MMF harmonic spectrum of the dual three phase with different shift angles. Observe that 1st harmonic is eliminated by the 15° configuration and 5th and 7th are eliminated by the 30° configuration, which are consistent with the above analysis. The winding factor of 11th harmonic is also increased, which can improve torque density. Meanwhile, the torque ripple of the dual three-phase system is lower than that of the three-phase system. This is attributed to the phase offset of the torque waveforms produced by the two winding sets. Thus, the torque ripple is significantly eliminated [26]. It is predicted that the 30° configuration will have the best torque performance compared to its counterparts.

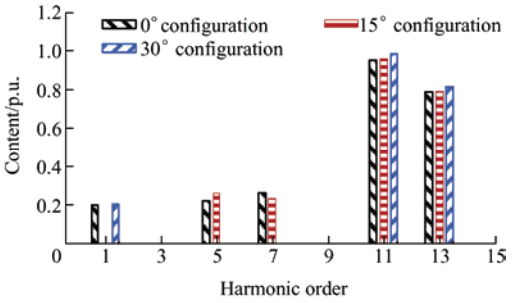

Fig. 3 Winding MMF harmonic analysis of dual three phase

2.2 Permeance

The stator slotting effect causes an uneven permeance distribution along the air gap, which can modulate the PM and winding of MMFs. The stator permeance can be expressed as

$$\Lambda_s(\theta_s)=\Lambda_{s0}+\sum_{m=1,2,\cdots}^{\infty}\Lambda_{sm}\cos(mN_s\theta_s) \tag{6}$$

where Λ_{s0} and Λ_{sm} are the DC component and the amplitude of the m^{th} order harmonic, respectively. N_s is the number of stator FMPs and is equal to 48. m is a positive integer.

For the DPMEVM, the rotor iron can also modulate the magnetic fields, and the rotor permeance can be expressed as

$$\Lambda_r(\theta_s,t)=\Lambda_{r0}+\sum_{n=1,2,\cdots}^{\infty}\Lambda_{rn}\cos nP_{rpm}(\theta_s-\omega_r t) \quad (7)$$

where Λ_{r0} and Λ_{rn} are the DC component and amplitude of the n^{th} order harmonic, respectively. n is positive integer. P_{rpm} is the number of rotor pole pairs and is equal to 37.

2.3 Air gap flux density

In DPMEVMs, the winding MMF can be modulated by both rotor and stator permeance. Therefore, the air gap flux density of the armature field can be expressed as

$$\begin{aligned}B&=F_s\times\Lambda_s\times\Lambda_r=\Lambda_{s0}\Lambda_{r0}F_s+\\&\frac{1}{2}\Lambda_{s0}\sum_{h}^{\infty}\sum_{n=1,2,\cdots}^{\infty}\Lambda_{rn}F_h\cos(h\pm nP_{rpm})(\theta_s-\frac{(1\pm n)p_r\omega_r t}{h\pm nP_{rpm}})+\frac{1}{2}\Lambda_{s0}\sum_{h}^{\infty}\sum_{n=1,2,\cdots}^{\infty}\Lambda_{rn}F_h\cos(k\pm nP_{rpm})(\theta_s+\frac{(1\mp n)p_r\omega_r t}{k\pm nP_{rpm}})+\\&\frac{1}{2}\Lambda_{r0}\sum_{h}^{\infty}\sum_{m=1,2,\cdots}^{\infty}\Lambda_{sm}F_h\cos(h\pm mN_s)(\theta_s-\frac{p_r\omega_r t}{h\pm mN_s}))+\frac{1}{2}\Lambda_{r0}\sum_{h}^{\infty}\sum_{m=1,2,\cdots}^{\infty}\Lambda_{sm}F_h\cos(k\pm mN_s)(\theta_s+\frac{p_r\omega_r t}{(k\pm mN_s)})+\\&\frac{1}{4}\sum_{h}^{\infty}\sum_{m=1,2,\cdots}^{\infty}\sum_{n=1,2,\cdots}^{\infty}\Lambda_{rn}\Lambda_{sm}F_h\cos(nP_{rpm}\pm mN_s\pm h)(\theta_s-\frac{(n\pm1)P_{rpm}\omega_r t}{nP_{rpm}\pm mN_s\pm h})+\\&\frac{1}{4}\sum_{k}^{\infty}\sum_{m=1,2,\cdots}^{\infty}\sum_{n=1,2,\cdots}^{\infty}\Lambda_{rn}\Lambda_{sm}F_k\cos(nP_{rpm}\pm mN_s\pm k)(\theta_s-\frac{(n\mp1)P_{rpm}\omega_r t}{nP_{rpm}\pm mN_s\pm k})\end{aligned} \quad (8)$$

Observe from the equation that there are many types of harmonics in the air gap. One part of the harmonics is the original harmonic of h^{th} (or k^{th}) produced by the winding MMF, which is not modulated. Meanwhile, the winding MMF can be modulated by the rotor and stator separately, and generates harmonics of $|h(k)\pm mN_s|$ and $|h(k)\pm np_{rpm}|$. The remaining harmonics are modulated by both the rotor and stator permeance. However, their content is very small and can be ignored. In a PMSM, only the stator permeance can modulate the MMF. Therefore, except for the original harmonics of h^{th} (or k^{th}), there also exist modulated harmonics of $|h(k)\pm mN_s|$. The harmonics and corresponding speeds of the armature reaction flux density are listed in Tab. 2.

Tab. 2 Modulated armature reaction field harmonic

Permeance	Harmonic order	Speed
Stator	$\lvert h\pm mN_s\rvert$	$\frac{p_{rpm}\omega_r}{h\pm mN_s}$
	$\lvert k\pm mN_s\rvert$	$-\frac{p_{rpm}\omega_r}{k\pm mN_s}$
Rotor	$\lvert h\pm np_{rpm}\rvert$	$\frac{p_{rpm}\omega_r\pm np_{rpm}\omega_r}{h\pm np_{rpm}}$
	$\lvert k\pm np_{rpm}\rvert$	$-\frac{np_{rpm}\omega_r\pm p_{rpm}\omega_r}{k\pm np_{rpm}}$

PM MMFs can also consider the modulation of the stator and rotor. For the rotor PM field, the air gap flux density B_{rpm} can be expressed as

$$\begin{aligned}B_{rpm}&=F_{rpm}\times\Lambda_s=\Lambda_{s0}\sum_{j}^{\infty}F_j\cos jp_{rpm}(\theta_s-\omega_r t)+\\&\frac{1}{2}\sum_{m=1,3,5}^{\infty}\sum_{j}^{\infty}F_j\Lambda_{si}\cos((jp_{rpm}\pm mN_s)(\theta_s-\frac{jp_{rpm}\omega_r t}{jp_{rpm}\pm mN_s}))\end{aligned} \quad (9)$$

After the modulation of the stator, apart from the original harmonics of jp_{rpm}, there also exist harmonics of $|jp_{rpm}\pm mN_s|$, which are modulated by the stator FMPs.

For the stator PM field in the DPMEVMs, the air-gap flux density B_{spm} can be expressed as

$$\begin{aligned}B_{spm}&=F_{spm}\times\Lambda_r=\Lambda_{r0}\sum_{j=0,1,2,3,\cdots}^{\infty}F_{sj}\cos jZ\theta_s+\\&\frac{1}{2}\sum_{j=0,1,2,3,\cdots}^{\infty}\sum_{n=1,2,\cdots}^{\infty}\Lambda_{rn}F_{sj}\cos(nP_{rpm}\pm jZ)(\theta_s-\frac{nP_{rpm}\omega_r t}{nP_{rpm}\pm jZ})\end{aligned} \quad (10)$$

In addition to the original harmonics of jZ, there also exist modulated harmonics of $|np_{rpm}\pm jZ|$. The detailed attributes of the modulated harmonics and speed of the stator and rotor PM are listed in Tab. 3.

Tab. 3 Modulated PM field harmonic

MMF	Harmonic order	Speed
Rotor PM	$\lvert jp_{rpm}\pm mN_s\rvert$	$\frac{np_{rpm}\omega_r}{jp_{rpm}\pm mN_s}$
Stator PM	jZ	0
	$\lvert np_{rpm}\pm jZ\rvert$	$-\frac{np_{rpm}\omega_r}{np_{rpm}\pm jZ}$

2.4 Torque production mechanism

According to the classical electromagnetic theory, steady torque can be produced when the armature reaction magnetic and PM field harmonics satisfy the following conditions.

(1) They have the same pole pairs and speed and can produce steady torque. Notice that the PMSM has the same rotor and winding pole pairs and corresponding speed, which can produce a steady torque.

(2) The same pole pairs and speeds are not present in the two magnetic fields, but there are FMPs between them. The same-order harmonics in the modulated PM and winding magnetic fields are called working harmonics. A steady torque can be produced by the interaction between the working harmonics. In DPMEVMs, many working harmonics can improve torque density.

2.5 Torque ripple reduction principle

According to Ref. [27], the electromagnetic torque can be expressed as

$$\begin{cases} T = T_{all\_av} + T_{all\_rip} \\ T_{all\_rip} = p\sum_{n=1}^{\infty} T_{prn}\sin\left(N_{ps}n\theta_s\right) \end{cases} \tag{11}$$

where T is the electromagnetic torque, T_{all_av} is the average torque, T_{all_rip} is the torque ripple, T_{prn} is the coefficient of n^{th} order harmonic torque ripple. p is the pole-pair number, N_{ps} is the least common multiple of the slot and pole-pairs number.

Under unsaturated conditions, the torque of the DPMEVMs can be considered as the superposition of the torque generated by the stator PMs and rotor PMs. To reduce the torque ripple of a conventional DPMEVM, magnets shifting in the stator is proposed in this paper. As shown in Fig. 1c, all stator PMs are shifted by β °. The torque ripple of stator-sided PMs after magnets shifting can be expressed as

$$T_{all\_rip} = p_{spm}\sum_{n=1}^{\infty} T_{prn}\sin N_{ps}n\left(\theta_s - \beta\right) \tag{12}$$

In general, the phase angle of the torque generated by stator-sided PMs can be shifted by β°. Hence, the phase angle between the two torque components of the DPMEVM can be varied. Subsequently, the torque ripple can be reduced because of the mutual compensation of the two torque components.

3 Comparison and evaluation

In this section, the electromagnetic performances of the three machines are analyzed and compared. For a fair comparison, the major parameters of the proposed machines were set identical to those of the baseline machine. In addition, the PM consumption of proposed machines I and Ⅱ were kept the same.

3.1 Flux density

Compared with the baseline machine, the proposed machines have complex air gap magnetic fields owing to the two PMs sets and rotor salient poles. Fig. 4 shows the no-load air gap flux density of rotor-side PMs, stator-side PMs, and both stator-and rotor-side PMs of the proposed machine I. The no-load air gap flux density of the DPMEVMs can be divided into the stator flux density and rotor flux density. As depicted in Fig. 4a, high-content harmonics are generated by the stator PM MMF, namely, 24$^{\text{th}}$, 48$^{\text{th}}$, and 72$^{\text{nd}}$ orders. The 24$^{\text{th}}$ and 48$^{\text{th}}$ harmonics can be modulated by the rotor permeance to the 11$^{\text{th}}$, 13$^{\text{th}}$, 61$^{\text{st}}$, and 85$^{\text{th}}$ orders. Observe from Fig. 4b that the 37$^{\text{th}}$ harmonic has the maximum amplitude because of the large number of rotor PMs. The stator permeance can also modulate the PM MMF and generate the 11$^{\text{th}}$ and 85$^{\text{th}}$ harmonics, which can be calculated according to Tab. 3. As shown in Fig. 4c, the harmonics of proposed machine I are the superposition of harmonics generated by both stator-and rotor-side PMs.

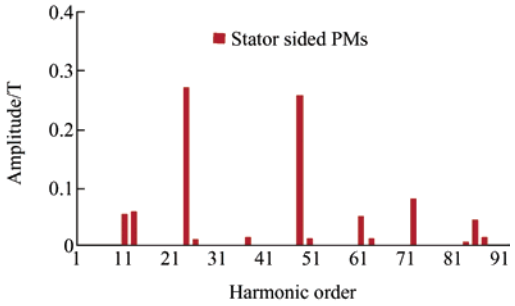

(a) Stator sided PMs

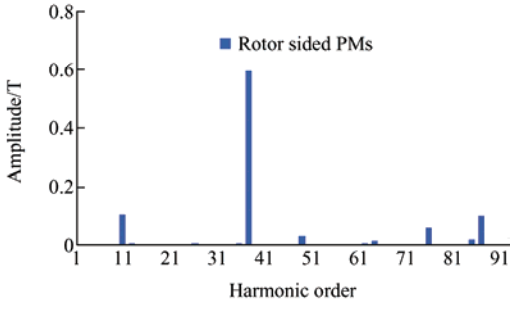

(b) Rotor sided PMs

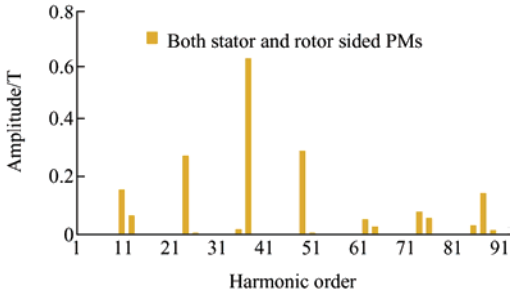

(c) Both stator and rotor sided PMs

Fig. 4 Spectra of no-load air gap flux density in proposed machine I

Fig. 5 shows the spectrum of no-load air gap flux density in proposed machine Ⅱ and baseline machine, respectively. As shown in Fig. 5a, the proposed machine Ⅱ has the same harmonics with the proposed machine I. The difference is that the amplitude of the harmonics is changed. Observe from Fig. 5b that the primitive 11^{th} and 33^{rd} harmonics are generated by rotor sided PMs. The modulated harmonics are generated by the stator modulation, e.g. 13^{th}-, 35^{th}- and 37^{th}-orders. Compared with the proposed machines, the baseline machine only has rotor sided PMs, and the PM usage is large despite the 11th harmonic being significantly high. In DPMEVMs, the number of rotor-side PMs is larger than that of stator-side PMs; moreover, the amplitude of 37^{th} harmonic is much higher than 24^{th} and 48^{th} harmonic ones. This can produce a high output torque.

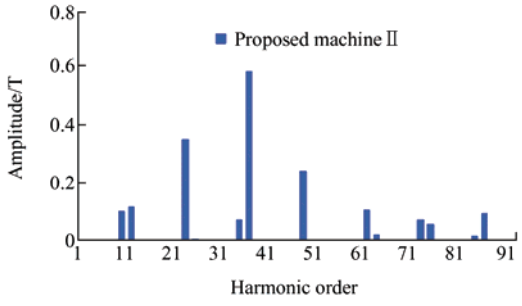

(a) Proposed machine Ⅱ

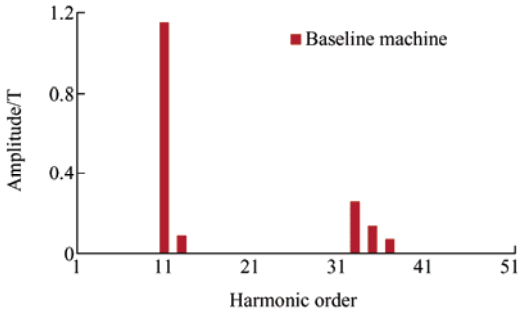

(b) Baseline machine

Fig. 5 Spectra of no-load air gap flux density

3.2 Back EMF

For the analyzed machines, the no-load back EMF can be expressed as

$$e_a = -\frac{\mathrm{d}}{\mathrm{d}t}\left[rl\int B(\theta_s,t)\sum_v N_v \cos(v\theta_s)\right] = r_g l \Lambda_{s0} N_{v=p}\pi\omega_r F_1 \cos(\omega_r t) + \frac{1}{2} r_g l \omega_r \pi \sum_{m=1,2,3}^{\infty} F_1 \Lambda_{si} N_{v=p\pm mN_s} \cos(\omega_r t) \quad (13)$$

where N_v is the winding factor, r_g is the air gap radius, l is the stack length, v is a positive constant. It is known that harmonics that satisfy the equation will contribute to the fundamental back EMF [28].

In DPMEVMs, both stator-and rotor-side PMs can produce a back EMF. The no-load back EMF of the proposed machines can be obtained by superimposing these two components. Fig. 6 shows the no-load back EMF produced by stator-side PMs, rotor-side PMs, and both in proposed machine I. As illustrated, the calculation results are consistent with the superposition relation. Fig. 7 plots the no-load back EMF of the analyzed machines. The waveforms of the proposed machines are more sinusoidal than that of the existing one. The fundamental amplitudes of the baseline machine, proposed machine I, and proposed machine Ⅱ are 71 V, 75.8 V, and 81.5 V, respectively.

The 3rd harmonic of the PMSM is higher than that of the two proposed machines, which leads to a potentially higher torque ripple.

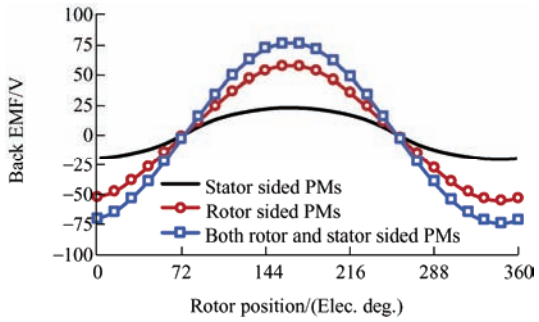

Fig. 6 No-load back EMF of proposed machine I

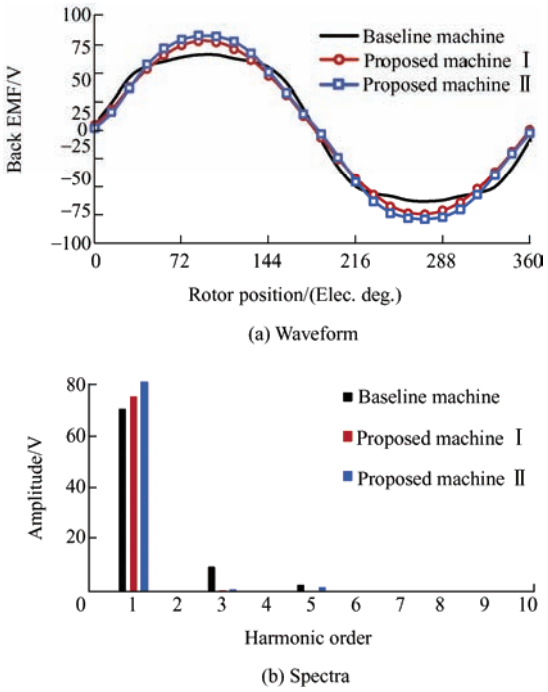

Fig. 7 No-load back EMF of the analyzed machines

3.3 Torque analysis

Fig. 8 illustrates the cogging-torque waveforms of the analyzed machines. The cogging torque of the baseline machine was higher than that of the proposed machine. Meanwhile, the cogging torque of proposed machine II can also be reduced after magnets shifting. The torque performances of the analyzed machines are compared in Fig. 9. The average torque of the baseline machine, proposed machine I and proposed machine Ⅱ is 61.4 N·m, 64.2 N·m and 68.8 N·m, respectively. The torque ripples were calculated to be 2.66%, 1.86%, and 0.86%, respectively. The torque ripple of the proposed machines is lower than that of the baseline machine. Furthermore, after the magnets shift, the torque ripple of the proposed machine II is reduced by more than 50% compared with the proposed machine I. Meanwhile, the material consumption owing to the PM in the proposed machines I and Ⅱ is 62% of the existing one, which can reduce manufacturing costs.

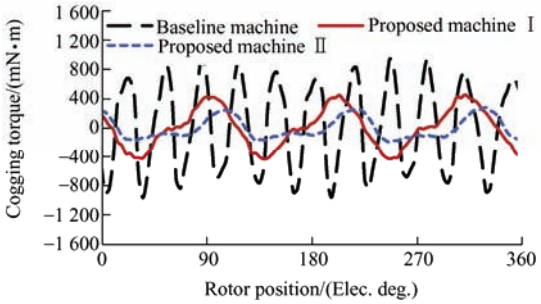

Fig. 8 Cogging torque comparison of the analyzed machines

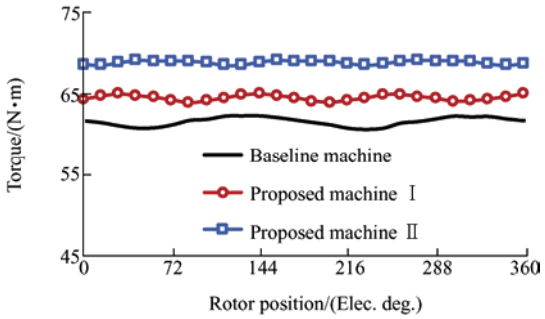

Fig. 9 Torque performance comparison of the analyzed machines

In contrast to the baseline machine, the proposed machines are operated based on multiple working harmonics, which can enhance the torque density. According to Tabs. 2 and 3, the working harmonics of the proposed machines can be identified. The torque contribution of dominant field harmonics can also be investigated using the Maxwell stress tensor.

The electromagnetic torque produced by the k^{th} radial and tangential air gap field flux harmonics can be derived from Ref. [29].

$$T_k(t)=\frac{\pi r^2 l_{ef}}{\mu_0}B_{rk}B_{tk}\cos(\theta_{rk}-\theta_{tk}) \tag{14}$$

where r is the air gap radius, μ_0 is the vacuum permeability, l_{ef} is the effective axial length. B_{rk} and B_{tk} are the k^{th} Fourier coefficients of B_r and B_t, respectively. θ_{rk} and θ_{tk} are the corresponding phases.

Tab. 4 lists the working harmonics of the proposed machines and their corresponding speeds. Meanwhile, the torque proportion contributed by each working harmonic in proposed machine Ⅰ is also listed in Tab. 4. Notice that the working harmonics comprise three

types of speeds: positive, negative, and zero. The speeds of 13th, 37th, 61st, 74th, and 85th harmonics are positive and rotate in the same direction as the rotor. The speeds of the 11th and 35th harmonics are negative. The speeds of the 24th, 48th, and 72nd harmonics are zero. Fig. 10 shows the phase-angle variation for each working harmonic. Observe that the rotation direction of the phase angle of each harmonic corresponds to the analysis reported in Tab. 4.

Tab. 4 Working harmonics and torque proportion

Harmonic order	Speed	Torque proportion(%)
11	$-37\omega_r/11$	–4.2
13	$37\omega_r/13$	5.8
24	0	10.7
35	$-37\omega_r/35$	0.98
37	ω_r	66.7
48	0	19.7
61	$37\omega_r/61$	0.28
72	0	–1.8
74	$2\omega_r$	–1.09
85	$37\omega_r/85$	0.38
Sum	—	97.45

Based on the air gap flux density and rotation position angle, the torque of each working harmonic can be calculated, as shown in Tab. 4. The torques produced by the 11th, 72nd, and 74th harmonics are negative with a minimal proportion. This is because the cosine value of the difference between the radial and tangential phase angles is negative. The remaining harmonics all contribute to the positive torque. As listed in Tab. 4, more than 97% of the electromagnetic torque in proposed machine I is contributed by the dominating harmonics. The torque produced by the 37th harmonic accounted for 66.7% of the total torque, which was the main working harmonic. The 24th and 48th harmonics produced 30.4% of the total torque. The torque produced by the remaining working harmonics is low. Observe that the dual PMs structure with multi working harmonics can improve the torque density.

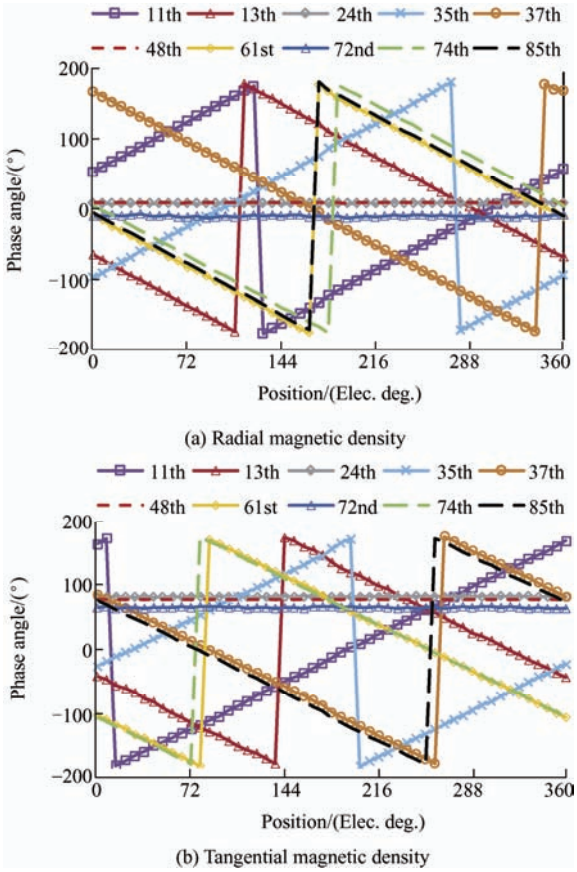

Fig. 10 Phase angle of each working harmonics of proposed machine I

3.4 Torque ripple reduction

The proposed machines are unsaturated and operate in a linear area. Hence, the two torque components can be superimposed directly to obtain the torque of the proposed machine. Fig. 11 shows the torque produced by the stator-side PMs and rotor-side PMs in proposed machine I. The average torque produced by the stator-side PMs is 19.8 N·m with a peak-to-peak value of 0.69 N·m. For the rotor-side PMs, the average torque and peak-to-peak values are 45.8 N·m and 0.64 N·m, respectively. Note that the superposition of torque generated by the stator and rotor PM is 65.6 N·m, which corresponds to the torque of the proposed machine I. However, it should be noted that the phase angle between the two torque components is close. The peak-to-peak values of the two torques also satisfy the superposition relation, which causes a high torque ripple in proposed machine I.

In order to reduce the torque ripple of the proposed machine I, the phase angle between the two torque components can be changed to reduce the torque ripple.

The magnets shifting in the stator is applied in the proposed machine Ⅱ. Hence, after the magnets shifting, the peak-to-peak value of the torque can be reduced by the mutual compensation of the two torque components. Subsequently, the torque ripple is reduced. The shifting angle β should be greater than half of the torque-fluctuation period. The torque ripple of proposed machine Ⅱ under different shifting angles is shown in Fig. 12. After the magnet shifts, the torque ripple can be reduced because of the mutual compensation of the two torque components. Moreover, with an increase in the shifting angle, the torque ripple first decreases and then increases. Notice that the torque ripple can be reduced by more than 50% when β is 0.75 °. Fig. 13 shows the torque performance of the rotor-sided PMs and stator-side PMs in the proposed machine Ⅱ after magnets shifting in stator. Notice that after magnets shifting, the phase angle of the torque is shifted. Obviously, the peak of the torque generated by the stator-side PMs corresponds to the trough of the torque generated by the rotor-side PMs. Thus, the torque ripple can be significantly reduced. It is verified that the proposed machine Ⅱ can obtain a low torque ripple owing to magnets shifting. The average torque is also improved.

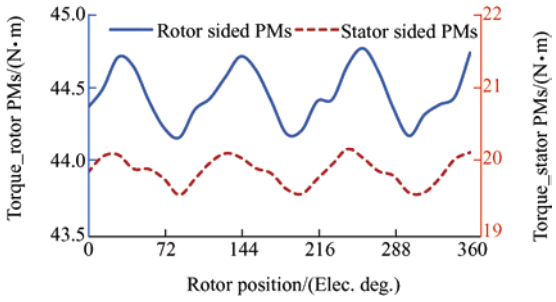

Fig. 11 Torque produced by different sided PMs in proposed machine I

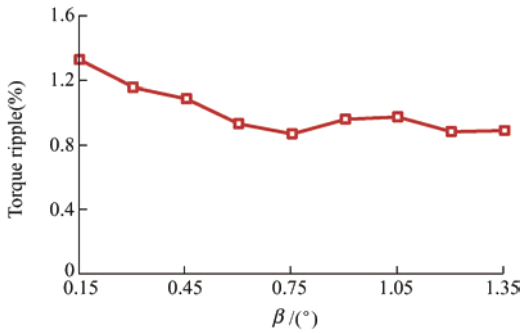

Fig. 12 Torque ripple under different shifting angle

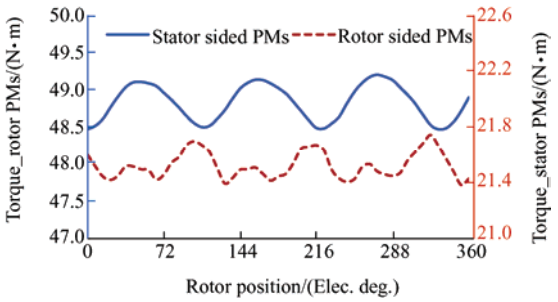

Fig. 13 Torque produced by different sided PMs in proposed machine Ⅱ

3.5 High-torque application

Based on the above analysis, notice seen that the DPMEVMs can obtain the same average torque as PMSMs while reducing the PM material usage. The revealed principle can be extended to machines with the same unit motor of 24s-22p. The electromagnetic performance of the PMSMs and DPMEVMs exhibit the same trend when they use the same unit motor of 24s-22p.

The 120s-110p models of the PMSM and DPMEVM are analyzed in this section. Fig. 14 shows the cross-sections of the baseline machine and the proposed machine. Tab. 5 lists the main parameters of the two machines. The unit motor of the two machines is 24s-22p. Meanwhile, the two machines adopt dual three-phase with a 30° phase shift to improve the torque performance. The 120 slots models can be seen as five times expansion of 24 slots models; thus, the electromagnetic performance of 120 slots models exhibit the same trends as the unit motor. The working harmonics of 120 slots models can be easily obtained according to the unit motor. The order of the working harmonics is five times that of the unit motor.

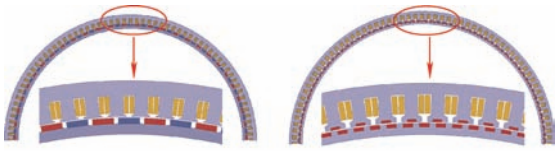

Fig. 14 Cross sections of the analyzed machines

Tab. 5 Parameters of two machines

Parameter	Baseline machine	Proposed machine
PM pole-pairs	55	185
Winding pole-pairs	55	
Stator outer diameter/mm	1 380	
Stator inner diameter/mm	1 280	
Axial length/mm	20	
Air-gap length/mm	2	

Fig. 15 shows the no-load back EMF of the analyzed machines. Observe that the waveform of the proposed machine is more sinusoidal than that of the baseline machine. The amplitude of the fundamental amplitude is 67.8 V and 72 V, for the baseline machine and proposed machine, respectively. The 3rd harmonic of the baseline machine is much higher than that of the proposed machine. Fig. 16 shows the torque performance of the analyzed machines. The average torques of the baseline machine and proposed machine are 1 044 N·m and 1 062.6 N·m, respectively. The torque ripples of the existing and proposed machines are 0.78% and 0.53 %, respectively. The PM material usage of the proposed machine is 75% of that of the baseline machine, which can significantly reduce manufacturing costs.

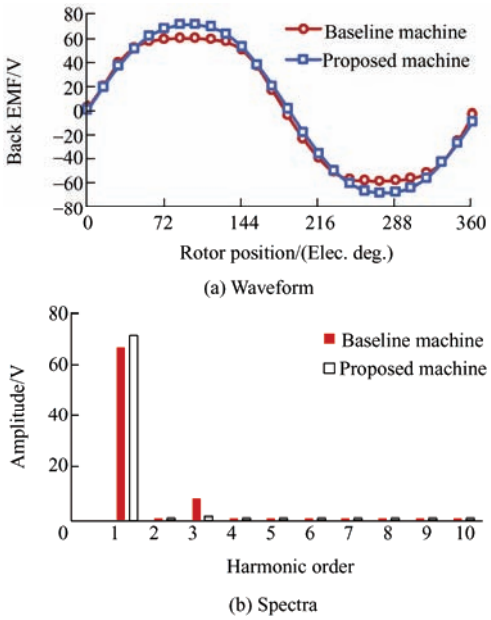

Fig. 15 No-load back EMF of the analyzed machines

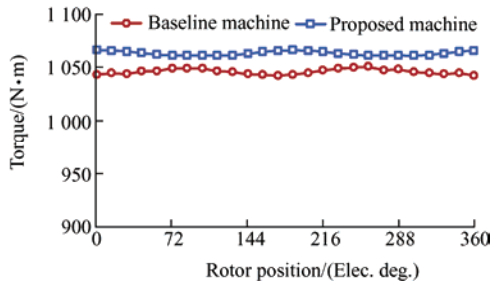

Fig. 16 Torque performance comparison of analyzed machines

4 Experimental validation

To verify the previous analyses further, a prototype of the PMSM was manufactured. Fig. 17 shows pictures of the prototype. The stator employs a modular structure to reduce manufacturing difficulties. The stator was divided into 10 modules, and each module had 12 stator slots. Meanwhile, several round holes were opened in the stator yoke to fix the stator on the pedestal. In fractional-slot concentrated winding motors, the flux mainly passes through the stator tooth. That is, the stator holes have no effect on the flux path. The gaps between the adjacent stator modules are minute, and their influence on the flux path can be ignored. Fig. 18 plots the no-load back EMF of the prototype. As depicted, the measured value is approximately 54.8 V. Fig. 19 illustrates the simulated and experimental no-load back EMF of the prototype machine. Observe that the measured back EMF is consistent with the simulated EMF.

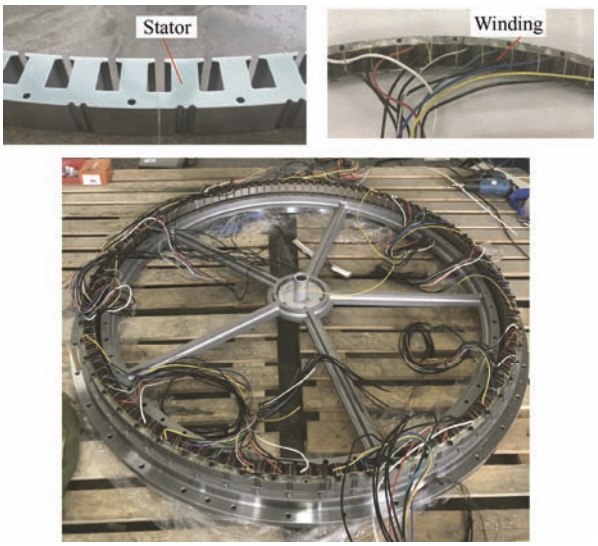

Fig. 17 Pictures of prototype

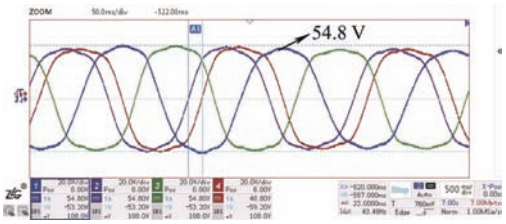

Fig. 18 No-load back EMF of prototype (50 ms/div, 20 V/div)

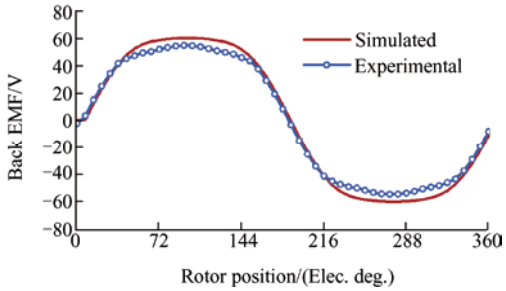

Fig. 19 Simulated and experimental no-load back EMF

5 Conclusions

In this study, a novel DPMEVM with magnets shifting in stator was proposed. The conventional PMSM and proposed DPMEVMs with a 24s-22p unit motor were compared and analyzed. Moreover, the harmonics of the three machines were analyzed from the air gap field modulation stand point. Subsequently, the working harmonics and their contributions to the torque were distinguished and calculated. Compared with the existing PMSM, the proposed DPMEVMs with efficient utilization of multi-working harmonics exhibit a higher torque density. The proposed DPMEVMs can reduce PM material usage by 38 % while reaching the same torque as the existing PMSMs. Furthermore, the torque ripple of the proposed machine Ⅱ was significantly reduced after the magnets shifting in stator. For high-torque applications, 120 slot models with the same unit motor of 24s-22p have been built and compared. It was demonstrated that the proposed DPMEVM machine could obtain improved torque capability compared with the existing PMSM machine. Finally, a prototype of the 120s-110p PMSM was manufactured and verified.

References

[1] X Chen, J Wang. Magnetomotive force harmonic reduction techniques for fractional-slot non-overlapping winding configurations in permanent-magnet synchronous machines. *Chin. J. Electr. Engin.*, 2017, 3(2): 102-113.

[2] H Zhang, W Hua, Z Wu. Modular spoke-type permanent-magnet machine for in-wheel traction applications. *IEEE Trans*. *Ind*. *Electron*., 2018, 65(10): 7648-7659.

[3] Y Yang, M M Rahman, T Lambert, et al. Development of an external rotor V-shape permanent magnet machine for E-bike application. *IEEE Trans*. *Energy Convers*., 2018, 33(4): 1650-1658.

[4] X Zhao, S Niu. A new slot-PM vernier reluctance machine with enhanced zero-sequence current excitation for electric vehicle propulsion. *IEEE Trans*. *Ind*. *Electron*., 2020, 67(5): 3528-3539.

[5] B Kim. Design method of a direct-drive permanent magnet vernier generator for a wind turbine system. *IEEE Trans*. *Ind*. *Appl*., 2019, 55(5): 4665-4675.

[6] Z Q Zhu, Y Liu. Analysis of air-gap field modulation and magnetic gearing effect in fractional-slot concentrated-winding permanent-magnet synchronous machines. *IEEE Trans*. *Ind*. *Electron*., 2018, 65(5): 3688-3698.

[7] M Cheng, P Han, W Hua. General air gap field modulation theory for electrical machines. *IEEE Trans*. *Ind*. *Electron*., 2017, 64(8): 6063-6074.

[8] M Cheng, Z Xu, M Tong, et al. Analysis and optimization of a five-phase hybrid excitation flux switching machine based on the consistency and complementarity principle. *Chin. J. Electr. Engin.*, 2021, 7(3): 52-64.

[9] W Li, T W Ching, K T Chau. Design and analysis of an outer-rotor parallel-hybrid-excited vernier machine. *Chin. J. Electr. Engin.*, 2017, 3(1): 27-32.

[10] L Xu, W Zhao, M Wu, et al. Investigation of slot-pole combination of dual-permanent-magnet-excited vernier machines by using air-gap field modulation theory. *IEEE Trans*. *Transp*. *Electrifi*c., 2019, 5(4): 1360-1369.

[11] X Ren, D Li, R Qu, et al. Investigation of spoke array permanent magnet vernier machine with alternate flux bridges. *IEEE Trans*. *Energy Convers*., 2018, 33(4): 2112-2121.

[12] A Nematsaberi, J Faiz. A novel linear stator-PM vernier machine with spoke-type magnets. *IEEE Trans*. *Magn*., 2018, 54(11): 8106905.

[13] D Li, R Qu, Z Zhu. Comparison of Halbach and dual-side vernier permanent magnet machines. *IEEE Trans*. *Magn*., 2014, 50(2): 7019804.

[14] L Wei, T Nakamura. A novel dual-stator hybrid excited permanent vernier machine with Halbach-array PMs. *IEEE Trans Magn*., 2021, 57(2): 20287788.

[15] H Qu, Z Q Zhu, H Li. Analysis of novel consequent pole flux reversal permanent magnet machines. *IEEE Trans*. *Ind*. *Appl*., 2021, 57(1): 20320283.

[16] H Wang, S Fang, H Yang, et al. A novel consequent-pole hybrid excited vernier machine. *IEEE Trans*. *Magn*., 2017, 53(11): 8112304.

[17] Y Liu, Z Q Zhu. Magnetic gearing effect in vernier permanent magnet synchronous machines. *Proc*. *IEEE Energy Convers*. *Congr*. *Expo*. (*ECCE*), 1-5 Oct. 2017, Cincinnati, OH, USA. IEEE, 2017: 5025-5032.

[18] K Xie, D Li, R Qu, et al. A new perspective on the PM vernier machine mechanism. *IEEE Trans*. *Ind*. *Appl*., 2019, 55(2): 1420-1429.

[19] L Xu, G Liu, W Zhao, et al. High-performance fault tolerant halbach permanent magnet vernier machines for safety-critical applications. *IEEE Trans*. *Magn*., 2016, 52(7): 8104704.

[20] S Chung, J Kim, B Woo, et al. A novel design of modular three-phase permanent magnet vernier machine with consequent pole rotor. *IEEE Trans*. *Magn*., 2011, 47(10): 4215-4218.

[21] H Yang, Z Q Zhu, H Lin, et al. Analysis of consequent-pole flux reversal permanent magnet machine with biased flux modulation theory. *IEEE Trans*. *Ind*. *Electron*., 2020, 67(3): 2107-2121.

[22] A Ishizaki, T Tanaka, K Takasaki, et al. Theory and optimum design of PM vernier motor. *Proc*. *IEE Int*. *Conf*. *Electr*. *Mach*. *Drives*, 11-13 Sep. 1995, Durham, UK. IET, 1995: 208-212.

[23] L Jian, Y Shi, C Liu, et al. A novel dual-permanent-magnet-excited machine for low-speed large-torque applications. *IEEE Trans*. *Magn*., 2013, 49(5): 2381-2384.

[24] K Xie, D Li, R Qu, et al. A novel permanent magnet vernier machine with halbach array magnets in stator slot opening. *IEEE Trans*. *Magn*., 2017, 53(6): 7207005.

[25] Q Wang, S Niu, L Yang. Design optimization and comparative study of novel dual-PM excited machines. *IEEE Trans*. *Ind*. *Electron*., 2017, 64(12): 9924-9933.

[26] P Xu, J H Feng, S Y Guo, et al. Analysis of dual three-phase permanent-magnet synchronous machines with different angle displacements. *IEEE Trans*. *Ind*. *Electron*., 2018, 65(3): 1941-1954.

[27] G Liu, X Du, W Zhao, et al. Reduction of torque ripple in inset permanent magnet synchronous motor by magnets shifting. *IEEE Trans*. *Magn*., 2017, 53(2): 8100713.

[28] H Zhang, H Yin, W Hua, et al. The mechanism analysis on open-circuit back-EMF in fractional-slot concentrated winding permanent magnet machines using air-gap field modulation theory. *IEEE Trans*. *Transp*. *Electrific*., 2021, 7(4): 2658-2670.

[29] M Zhou, X Zhang, W Zhao, et al. Influence of magnet shape on the cogging torque of a surface-mounted permanent magnet motor. *Chin. J. Electr. Engin.*, 2019, 5(4): 40-50.

Feilong Yan received the B.Sc. degree in Electrical Engineering from Henan University of Science and Technology, Luoyang, China, in 2018. He is currently working toward the M.Sc. degree in Electrical Engineering from Jiangsu University, Zhenjiang, China.

His research interests include machine design and electromagnetic field analysis.

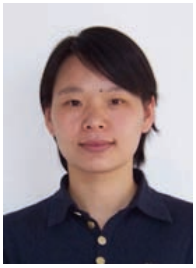

Jinghua Ji received the B.Sc., M.Sc., and Ph.D. degrees in Electrical Engineering from Jiangsu University, Zhenjiang, China, in 2000, 2003, and 2009 respectively. Since 2000, she has been with the School of Electrical and Information Engineering, Jiangsu University, where she is currently a Professor.

From 2013 to 2014, she was a Visiting Scholar with the Department of Electronic and Electrical Engineering, University of Sheffield, Sheffield, UK. Her areas of interest include motor design and electromagnetic field computation. She has authored and co-authored over 50 technical papers in these areas.

Zhijian Ling received the B.Sc. degree in Electrical Engineering and Automation from Shandong Agriculture University, Taian, China, in 2013, and the Ph.D. degree in Electrical Engineering from Jiangsu University, Zhenjiang, China, in 2020. He is currently a Lecturer with the School of Electrical and Information Engineering, Jiangsu University.

From September 2018 to August 2019, he was a joint Ph.D. student funded in the Department of Energy Technology, Aalborg University, Aalborg, Denmark. His research interests include the design and analysis of permanent magnet electrical machines, and electrical actuators.

Yuhua Sun received the B.Sc. degree in Electrical Engineering from Qilu University of Technology (Shandong Academy of Sciences), Jinan, China, in 2017. He is currently working toward the Ph. D. degree in Electrical Engineering at Jiangsu University, Zhenjiang, China.

His research interests include machine design and electromagnetic field analysis.

Wenxiang Zhao (M'08-SM'14) received the B.Sc. and M.Sc. degrees from Jiangsu University, Zhenjiang, China, in 1999 and 2003, respectively, and the Ph.D. degree from Southeast University, Nanjing, China, in 2010, all in Electrical Engineering.

He has been with Jiangsu University since 2003, where he is currently a Professor with the School of Electrical Information Engineering. From 2008 to 2009, he was a Research Assistant with the Department of Electrical and Electronic Engineering, University of Hong Kong, Hong Kong. From 2013 to 2014, he was a Visiting Professor with the Department of Electronic and Electrical Engineering, University of Sheffield, Sheffield, UK. His current research interests include electric machine design, modeling, fault analysis, and intelligent control. He has authored and co-authored over 200 technical papers in these areas.